Foreshock Properties at Typical and Enhanced Interplanetary Magnetic Field Strengths : Results From Hybrid-Vlasov Simulations

Turc, L.

2018-07

Turc , L , Ganse , U , Pfau-Kempf , Y , Hoilijoki , S , Battarbee , M , Juusola , L , Järvinen , R , Brito , T , Grandin , M & Palmroth , M 2018 , ' Foreshock Properties at Typical and Enhanced Interplanetary Magnetic Field Strengths : Results From Hybrid-Vlasov Simulations ' , Journal of geophysical research. Space physics , vol. 123 , no. 7 , pp. 5476-5493 . https://doi.org/10.1029/2018JA

http://hdl.handle.net/10138/242419
https://doi.org/10.1029/2018JA025466

acceptedVersion

Foreshock properties at typical and enhanced interplanetary magnetic eld strengths: results from hybrid-Vlasov simulations

L. Turc [1], U. Ganse [1], Y. Pfau-Kempf [1], S. Hoilijoki [1,2], M. Battarbee [1], L. Juusola [3,1], R. Jarvinen [2,4], T. Brito [1], M. Grandin [1] and M. Palmroth [1,3]

[1]Department of Physics, University of Helsinki, Helsinki, Finland
[2]Now at Laboratory for Atmospheric and Space Physics, University of Colorado, Boulder, USA
[3]Finnish Meteorological Institute, Helsinki, Finland
[4]Department of Electronics and Nanoengineering, School of Electrical Engineering, Aalto University, Espoo, Finland

Key Points:

- We study the e ects of the interplanetary magnetic eld strength on the foreshock properties using hybrid-Vlasov simulations
- The foreshock is structured over smaller scales for higher magnetic eld strength, waves are less monochromatic and grow in a larger region
- Suprathermal ion density decreases at higher eld strength and we identify a possible new signature of the foreshock compressional boundary

Corresponding author: Lucile Turc, lucile.turc@helsinki.fi

Abstract

In this paper, we present a detailed study of the e ects of the interplanetary magnetic eld (IMF) strength on the foreshock properties at small and large scales. Two simulation runs performed with the hybrid-Vlasov code Vlasiator with identical setup but with di erent IMF strengths, namely 5 and 10 nT, are compared. We nd that the bow shock position and shape are roughly identical in both runs, due to the quasi-radial IMF orientation, in agreement with previous magnetohydrodynamic simulations and theory. Foreshock waves develop in a broader region in the higher IMF strength run, which we attribute to the larger growth rate of the waves. The velocity of eld-aligned beams remains essentially the same, but their density is generally lower when the IMF strength increases, due to the lower Mach number. Also, we identify in the regular IMF strength run ridges of suprathermal ions which disappear at higher IMF strength. These structures may be a new signature of the foreshock compressional boundary. The foreshock wave eld is structured over smaller scales in higher IMF conditions, due to both the period of the foreshock waves and the transverse extent of the wave fronts being smaller. While the foreshock is mostly permeated by monochromatic waves at typical IMF strength, we nd that magnetosonic waves at di erent frequencies coexist in the other run. They are generated by multiple beams of suprathermal ions, while only a single beam is observed at typical IMF strength. The consequences of these di erences for solar wind-magnetosphere coupling are discussed.

1 Introduction

Shocks are ubiquitous in our universe, from planetary bow shocks to supernova remnants. One key parameter controlling the properties of a magnetized shock is its obliquity, quanti ed by the angle $_{Bn}$ between its normal direction and the upstream magnetic eld. The nature of the shock transition changes dramatically depending on whether the shock is quasi-perpendicular ($_{Bn} > 45$) or quasi-parallel ($_{Bn} < 45$). This stems from the fact that in the latter case particles re ected at the shock front can escape far upstream along the magnetic eld lines. The upstream region magnetically connected to a shock, which is populated by particles re ected o the shock front, is called the foreshock. The interaction of the backstreaming population with the incoming solar wind triggers plasma instabilities, resulting in the development of intense wave activity, in particular in the ultra-low frequency (ULF) range, from 1 mHz to 10 Hz. Spacecraft observations in the Earth's ion foreshock have evidenced the presence of 1 Hz, 3 s, 10 s and 30 s waves, as well as shocklets and discrete wave packets [e.g.Hoppe et al., 1981;Greenstadt et al., 1995;Burgess, 1997;Eastwood et al., 2003, 2005a;Hobara et al., 2007;Wilson III, 2016, and references therein].

The 30 s waves have been extensively studied, particularly because of the long standing question of their observed oblique propagation, while theory predicts that they should propagate preferentially parallel to the magnetic eld [eg.Gary, 1991;Eastwood et al., 2005b;Hsieh and Shue, 2013;Palmroth et al., 2015]. They are found in conjunction with intermediate, gyrophase-bunched or gyrotropic ion distributions [Eastwood et al., 2005]. The 30 s waves are quasi-monochromatic fast magnetosonic waves generated via the ion-ion beam right-hand instability [Gary, 1991]. They are right-hand polarized in the plasma frame and propagate with the ion beam, but because they are advected back to the bow shock by the solar wind ow, they appear as left-handed in the spacecraft frame [Eastwood et al., 2005a]. Their wavelength parallel to the magnetic eld is about R_E (Earth radius = 6371 km) [Hoppe and Russell, 1983;Archer et al., 2005]. The transverse extent of the wave fronts is much larger, of the order of 8 to 12 R_E [Archer et al., 2005]. Despite being called "30 s" waves, their period actually ranges between 10 and 55 s in the terrestrial foreshock [Eastwood et al., 2005]. They have also been detected at other planetary foreshocks, such as Mercury, Venus and Jupiter, where their frequency is roughly proportional to the interplanetary magnetic eld (IMF) strength, with $f \quad 0{:}006B$(nT) [Hoppe and Russell, 1982]. Subsequent studies have shown that the IMF cone angle, $_{Bx}$, between the IMF vector and the Sun-Earth

line, is another factor controlling the wave period [Takahashi et al., 1984; Le and Russell, 1996].

The edge of the ion foreshock is de ned as the limit beyond which no counterstreaming ion beams are observed. Because of the drift due to the solar wind motional electric eld, this boundary is located earthward of the tangent eld line and is inclined toward the bow shock. Inward of the foreshock edge, eld-aligned beams are observed, but no wave activity. This is due to the nite growth time of the instability, which has not yet had time to grow in this region as the beams have not interacted long enough with the solar wind [Blanco-Cano et al., 2009]. The ULF foreshock boundary marks where ULF waves start to develop [Eastwood et al., 2005a; Andrés et al., 2015]. More recent simulations and observations have evidenced another boundary deeper in the foreshock, where ULF waves become significantly compressive, termed the foreshock compressional boundary [Omidi et al., 2009; Rojas-Castillo et al., 2013]. The ULF foreshock is populated by intermediate, gyrotropic and gyrophase-bunched ion distributions, which become more and more distorted and have broader pitch angle distributions when moving toward the central foreshock. Di use distributions are detected in the vicinity of the bow shock [see, for example, Fuselier, 1995; Kempf et al., 2015; Wilson III, 2016, for more details on the ion distributions in the foreshock]. Overall, the density of suprathermal ions, independently of their velocity distribution function, decreases with increasing distance from the bow shock [Kis et al., 2004; Kempf et al., 2015]. In the eld-aligned beam region, the velocity of the backstreaming particles increases with increasing $_{Bn}$. It is therefore maximum at the foreshock edge and decreases toward the central foreshock [Burgess et al., 2012; Kempf et al., 2015] .

In addition to its substantial spatial variability, the foreshock varies also temporally, as its properties are intimately coupled with the changing solar wind conditions. The position of the quasi-parallel shock, and thus that of the foreshock, are directly controlled by the direction of the IMF [Francia et al., 2012; Turc et al., 2015]. The position of the foreshock boundaries is also dictated by the upstream solar wind conditions, in particular the IMF orientation, the solar wind velocity, but also the Alfvén Mach number (M_A) in the case of the foreshock compressional boundary [Eastwood et al., 2005a; Omidi et al., 2009; Andrés et al., 2015]. As mentioned above, the frequency of the ULF waves has been shown to depend on the IMF cone angle and strength [Le and Russell, 1996]. A decrease in the solar wind density results in a lower ULF wave activity [Le et al., 2000; Francia et al., 2012; Regi et al., 2014], while changes in the plasma can a ect the development of wave modes [Le et al., 1992; Hobara et al., 2007]. Enhanced uxes of energetic ions are observed at large solar wind speeds [see, e.g., Trattner et al., 1994; Kudela et al., 2005], suggesting that acceleration at the bow shock is more e cient under these conditions. Moreover, recent studies have shown that the 30 s waves in the magnetic eld are accompanied by oscillations of the energetic ion uxes when the solar wind velocity is above 400 km s^{-1} [Petrukovich et al., 2017].

However, each of these studies focuses on one speci c foreshock feature, and we are still missing the global picture of the consequences of a change in a given solar wind parameter. Such a study requires global kinetic simulations, since the magnetohydrodynamic description does not capture the foreshock, which is inherently a kinetic structure. Spacecraft measurements o er only a limited view of the foreshock and disentangling the temporal and spatial variations can be challenging, even more so in large statistical surveys. Numerical simulations o er the opportunity to isolate the e ects of a given solar wind parameter, thus facilitating the interpretation of the results. The foreshock has been extensively studied using hybrid-particle-in-cell (PIC) simulations [e.g., Omidi et al., 2005, 2013; Blanco-Cano et al., 2006, 2009; Karimabadi et al., 2014]. In the hybrid-PIC approach, ions are treated as macro-particles while electrons are considered as a uid. A large fraction of hybrid-PIC global studies are two-dimensional (2D) in real space, but 3D hybrid-PIC simulations of the foreshock have also been performed [Lin and Wang, 2005; Omidi et al., 2017]. An alternative is to model ions as velocity distribution functions, using the so-called hybrid-Vlasov formalism. This approach has been adopted in the Vlasiator code

(http://www.physics.helsinki. /vlasiator), which simulates the near-Earth space, including the foreshock, in its real physical scale von Alfthan et al., 2014]. Although being computationally heavy, the hybrid-Vlasov description has the advantage of providing noiseless ion velocity distribution functions. A number of studies utilizing this model have been already published and have shown a good agreement with previous numerical and observational works [Palmroth et al., 2015;Kempf et al., 2015;Hoilijoki et al., 2016;Pfau-Kempf et al., 2016;Hoilijoki et al., 2017;Palmroth et al., 2017].

In this paper, we will concentrate on the e ects of the IMF strength. This parameter is likely to in uence signi cantly the foreshock properties because it directly controls the bow shock strength, quanti ed by the upstream magnetosonic Mach number, which in turn a ects particle re ection at the shock front. It can also impact wave activity, since the plasma is proportional to the IMF magnitude. Using the Vlasiator simulation model, we will compare the foreshock properties at two di erent IMF magnitudes, 5 nT, corresponding roughly to its typical value at Earth, and 10 nT, which is comparable to the magnetic eld strength during geoe ective solar wind transients such as interplanetary coronal mass ejections, magnetic clouds and corotating interaction regions. The manuscript is organized as follows: the simulation model is described in Section 2 and the comparison of the two runs is presented in detail in Section 3. We summarize and discuss our results in Section 4.

2 Description of the model

Vlasiator is a hybrid-Vlasov simulation code targeted at global modeling of the terrestrial magnetosphere and its interaction with the solar wind while retaining ion kinetic physics [von Alfthan et al., 2014]. In the hybrid-Vlasov approach, ions are described as velocity distribution functions, while electrons are considered as a massless charge-neutralizing uid. The evolution of the system is obtained by solving the Vlasov equation, self-consistently coupled with Maxwell's equations. Closure is provided by the generalized Ohm law, with the Hall term included. A detailed description of the model can be found in von Alfthan et al. [2014] and Pfau-Kempf [2016]. The main advantage of the hybrid-Vlasov approach is that it does not rely on statistical sampling of the phase space, as is done in PIC simulations [e.g. Omidi et al., 2005;Blanco-Cano et al., 2006;Karimabadi et al., 2014], but provides a noiseless description of the ion velocity distribution functions. Also, the full geomagnetic dipole strength can be used in Vlasiator. Both temporal and spatial scales in the simulation are therefore directly comparable to those observed in the near-Earth space. The drawback to this approach is however the heavy computational cost of the runs, which have been so far limited to ve dimensions, two in real space and three in velocity space (2D3V).

In this paper, we analyze two Vlasiator runs with identical setup, with the exception of the IMF strength, set to 5 nT in the rst run, hereafter referred to as Run 1, and to 10 nT in the second run, Run 2. The IMF makes a 5 angle with the x-axis, being in a so-called quasi-radial orientation. Consequently, the foreshock develops upstream of the subsolar bow shock and is particularly prominent in these conditions. The corresponding IMF components are $\mathbf{B}(\text{Run 1}) = (-4.98, 0.44, 0)$ nT and $\mathbf{B}(\text{Run 2}) = (-9.96, 0.87, 0)$ nT. Since the magnetic eld is almost aligned with the solar wind ow, the solar wind motional electric eld does not play a signi cant role in these runs. A rst series of results from Run 1 has been presented in Palmroth et al. [2015], showing in particular that the simulation reproduces accurately the foreshock ULF wave properties. The following steady solar wind conditions are used in both runs: solar wind velocity $\mathbf{V} = (-600, 0, 0)$ km s^{-1}, ion density $n_{SW} = 3.3$ cm^{-3} and ion temperature $T = 500$ kK. These parameters are representative of fast solar wind conditions encountered regularly at Earth. The corresponding Alfvén Mach numbers are $M_A(\text{Run 1}) = 10$ and $M_A(\text{Run 2}) = 5$. The change in the IMF strength also a ects the plasma , i.e. the ratio of the thermal pressure to the magnetic pressure, which is equal to 2.8 in Run 1 and decreases to 0.57 in Run 2.

The runs are 2D in real space covering the x y plane, corresponding to the Geocentric Solar Ecliptic (GSE) equatorial plane; all vector quantities will be given hereafter in this coordinate system, unless stated otherwise. A 3D velocity space is self-consistently coupled with each ordinary space cell. The resolution in ordinary space is $x = 227$ km, that is, 1.8 solar wind ion inertial lengths, and in velocity space $v = 30$ km s^{-1}. The simulation box extends from 7 to 63.6 R_E along x and ± 31.3 R_E along y. The solar wind flows into the simulation domain from the $+x$ boundary, while copy conditions are applied to the $\pm x$ and $\pm y$ walls, meaning that the velocity distribution functions and magnetic fields inside the boundary are copied from the nearest cell inside the simulation domain, thus ensuring a smooth outflow. The inner boundary is located at about 5 R_E from the Earth's center and is treated in these runs as a perfect conductor. The simulation was run for 685 s in Run 1 and 539 s in Run 2. As a side note, the quasi identical setup of the two runs allowed us to assess the improvement of the code performance, as Run 1 was performed in 2014 and Run 2 in 2017. Run 2 ran about two to three times faster than Run 1, due to the implementation of more efficient solvers [Pfau-Kempf, 2016], thus showing the potential of Vlasiator to eventually run in 6D (i.e. 3D3V) with further improvements.

Previous studies have shown that Vlasiator reproduces well ion acceleration in the foreshock [Kempf et al., 2015] and in the magnetosheath [Palmroth et al., 2018], up to several tens of keV. Note however that to achieve global simulations, a sparse velocity grid has been implemented [von Alfthan et al., 2014], meaning that the most tenuous parts of the velocity space are discarded. The most energetic ions may therefore not be properly described. In terms of the wave frequency range, the main limitation comes from the spatial and temporal resolution of the simulation, which limit the steepening of the waves and the development of high-frequency oscillations such as the whistler wave packets commonly observed near the quasi-parallel bow shock [Pfau-Kempf et al., 2018]. In the present study, we will therefore concentrate on waves at periods above 1 s, which are properly described in the current runs.

3 Results

3.1 Large-scale structure of the foreshock

Figures 1a and 1b show color maps of the plasma density in the simulation domain of Run 1 and 2 at $t = 500$ s from the beginning of the runs. This time step was selected because the foreshock is well developed but the waves have not yet reached the inflow boundary. Note that because of the 2D configuration, the IMF piles up in front of the magnetosphere, causing the bow shock to move outward as time progresses. However, this effect is limited here because of the quasi-radial IMF configuration, and takes place at comparable rates in both runs, thus allowing the comparison of the foreshocks at a given time in the simulation. The color scale is identical in both panels and has been chosen so as to best highlight the foreshock waves, which extend up to about $x = 60$ R_E. The white (panel a) and purple (panel b) contours are plotted where $n = 2n_{SW}$ and their rightmost part is a good approximation of the bow shock position. Figures 1a and 1b evidence that the overall structure of the foreshock differs strikingly from Run 1 to Run 2. In Run 1, the wave fronts are coherent over rather large distances perpendicular to the solar wind flow and are organized around two spines [Palmroth et al., 2015]. In Run 2, however, the planar wave fronts are much smaller and the foreshock is structured at finer scales. This is probably related to the period of the foreshock waves being shorter in Run 2, as can readily be seen on these plots and will be analyzed in more detail in Section 3.3.

In order to ease the comparison of the large-scale structure of the foreshock in the two runs, we plot in Figure 1c some of its characteristic features in both simulations, namely the bow shock position (solid black and purple lines), the edges of the foreshock (dashed black and purple lines), i.e. the limit of the region where field-aligned ion beams are observed, and contours of B_z depicting the ULF foreshock, B_z being set to zero in the solar wind, the deviations from this value illustrate well the presence of foreshock waves. The contours are

Figure 1. Top panels: ion density in the equatorial plane in Run 1 (a) and Run 2 (b) at time $t = 500$ s from the beginning of the runs. The color scale is chosen so as to best highlight the foreshock waves. The white/purple contours mark where $n = 2n_{SW}$ and illustrate the bow shock position. The plus signs indicate the positions of virtual spacecraft used in Section 3.3. Bottom panel: large-scale structure of the foreshock in both runs. Black and purple solid lines: bow shock position. Black and purple dashed lines: foreshock edge. Blue/red and pink/green contours: ULF foreshock waves illustrated by contours of B_z at 0.5 nT.

drawn at $B_z = 0.5$ nT (red and pink) and $B_z = -0.5$ nT (blue and green). The bow shock shape and position are similar in both runs, despite the fact that M_A changes by a factor of two. Previous works, based on magnetohydrodynamic (MHD) theory [Cairns and Grabbe, 1994] and simulations [Chapman and Cairns, 2004], have predicted that the bow shock position becomes less sensitive to changes in M_A when θ_{Bn} tends toward zero, and lower M_A values have to be reached before the sunward retreat of the bow shock is observed. The similar bow shocks in our runs are thus due to the quasi-radial orientation of the IMF accompanied by rather high M_A values. As θ_{Bn} increases when moving toward the flanks, the bow shock of Run 2 lies there slightly farther from Earth than that of Run 1, consistent with the change in M_A. Our simulations thus support the predictions of MHD regarding the response of the quasi-parallel bow shock to changes in the upstream M_A.

Because of the comparable bow shock shapes in both runs, the edges of the foreshock (dashed lines in Figure 1c) are also very similar. This happens since the extent of the region where ion reflection occurs is controlled by θ_{Bn}. The foreshock is marginally broader in Run 2 due to the slightly flatter bow shock shape, thus enabling ion reflection over a somewhat larger area. This however does not seem to be sufficient to explain the difference in the extent of the ULF foreshock in the direction perpendicular to the solar wind flow, evidenced by the blue/red (Run 1) and green/pink (Run 2) contours, which is significantly larger than the variation of the position of the foreshock edges. The ULF foreshock develops upstream of the quasi-parallel shock, whose shape is essentially identical in both runs, thus ruling out the shock geometry as a sufficient explanation for the broader ULF foreshock in Run 2. Also, we note that the expansion of the ULF foreshock into the upstream medium was faster in Run 2, reaching the inflow boundary of the simulation earlier than in Run 1 (not shown). This might be due to a difference in the growth rate of the instability giving rise to the ULF waves, which will be investigated in Section 3.3.

3.2 Suprathermal ion properties

We now concentrate on the properties of suprathermal ions in the foreshock. The moments of the suprathermal population are direct outputs from our simulation. They are computed from the 3D ion distribution function after excluding the solar wind core. This is done by removing the contribution of the part of the distribution function located within a sphere around the solar wind bulk velocity, with a $92.5\ \mathrm{km\,s^{-1}}$ radius, that is well above the solar wind thermal velocity $V_{th} = 70\ \mathrm{km\,s^{-1}}$. The moments of the suprathermal population are therefore well-defined in the field-aligned beam regions on either sides of the foreshock, as the beam is distinct enough from the solar wind core. In the central foreshock, and even more so when moving closer to the bow shock, where the distribution functions become more complex, the moments of the suprathermal population should be used with more caution.

Figure 2a displays the ratio of suprathermal ion velocities in Run 1 and Run 2. In the outer foreshock (grey areas in the dawn ($y < 0$) and dusk ($y > 0$) sides of the foreshock), populated mostly by field-aligned beams, the velocity of suprathermal ions is essentially identical in both runs. This is consistent with models of generation of the field-aligned beams via reflection at the quasi-perpendicular bow shock [Burgess et al., 2012], as the beam energy then only depends on the inflow velocity and the geometry of the shock encounter [e.g. Schwartz et al., 1983]. Here, the solar wind velocity is the same in both runs, and the shock geometry varies very little, hence the comparable velocities. In the central foreshock, where ULF waves develop, the suprathermal ion velocity may be higher in Run 1, but part of the suprathermal population may not be taken into account in the moment calculation in this region. It is thus difficult to draw any conclusions as to the effect of the modified IMF strength on the suprathermal ions in the central foreshock without looking in more detail at the ion distribution functions.

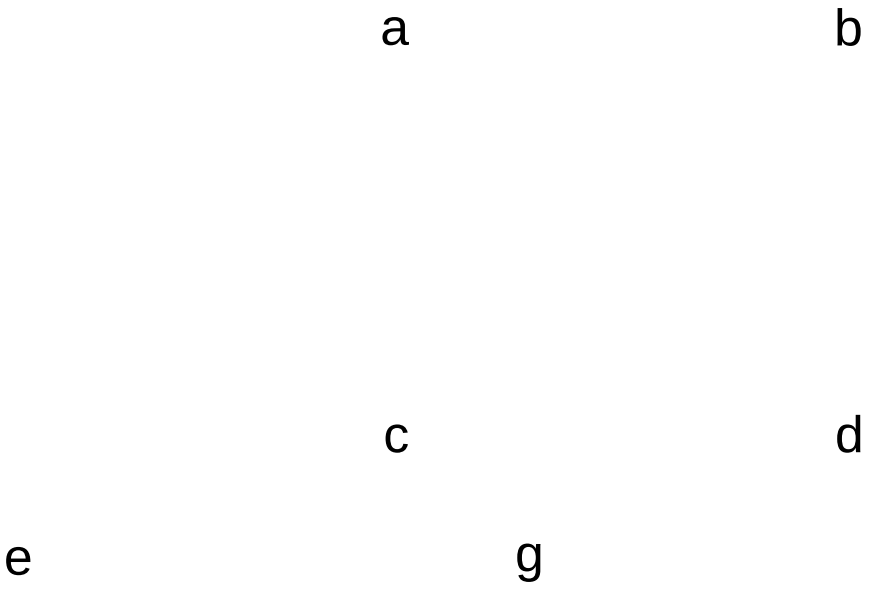

277 Figure 2. Ratio of the suprathermal ion velocities (a) and densities (b) in Run 1 and Run 2. Suprathermal
278 ion density in Run 1 (c) and Run 2 (d). The vertical black lines indicate the position of the cuts through the
279 foreshock displayed in Fig. 3. Ion time-energy spectrograms at position P1 = (x = 15.4 R_E, y = 15.2 R_E) and
280 P2 = (x = 15.4 R_E, y = 0.9 R_E) in Run 1 (panels e and f) and Run 2 (panels g and h).

The comparison of the suprathermal ion density (n_{beam}) in Run 1 and Run 2 is less straightforward. The ratio of this parameter in the two runs (Figure 2b) shows that in the outermost parts of the foreshock, the beam density is higher in Run 2 (in blue), while just outside of the ULF foreshock and in the central foreshock far from the shock, the opposite is observed (in green). To better illustrate the changes from one run to the other, we show the suprathermal ion density in Run 1 (Fig. 2c) and Run 2 (Fig. 2d). As the total ion density in Figure 1a and 1b, the color maps of suprathermal ion density reveal that the structuring of the foreshock operates at smaller scales in Run 2. Another major di erence between the two runs are the bands of enhanced n_{beam} which appear in Run 1 at the duskward and dawnward edges of the ULF foreshock (dark purple areas in Fig. 2c), but are absent in Run 2. They are most prominent closer to the bow shock, but remain visible throughout the simulation domain. These bands coincide with the green areas on either sides of the central foreshock in Fig. 2b, where the suprathermal ion density is a factor of 3 to 4 higher in Run 1 than in Run 2.

Panels e-h of Figure 2 show time-energy spectrograms at positions P1 and P2 in Run 1 (left) and Run 2 (right), where P1 is located in the region populated by eld-aligned beams and P2 in the ULF foreshock (as marked in Fig. 2c and d). On all spectrograms, the solar wind population is visible as a broad red band centered around 2 keV. The eld-aligned beam appears as a blue band around 8 keV in panels e and g. Its energy decreases slightly as time proceeds because the foreshock edge moves outward as the foreshock develops. At position P2, the distribution of suprathermal ions is much broader, extending from a few tens of eV to tens of keV, consistent with the di use ion population observed deep in the ULF foreshock [Fuselier, 1995]. We note that the solar wind core is partly disrupted. Furthermore, the ux of suprathermal ions is modulated. This is most visible between $t = 460$ s and $t = 490$ s in panel f, corresponding to a period of about 30 s, but a modulation at a shorter period, around 10 s, may also be present in panel h. This variation in the ux of suprathermal ions is similar to that reported by Petrukovich et al [2015] (see in particular Figure 4 of their paper), and is therefore likely caused by the foreshock ULF waves.

The top panel of Fig. 3 shows the suprathermal ion density along a cut perpendicular to the solar wind ow at $x = 30\ R_E$, as depicted by the vertical lines in Fig. 2c and d. When moving from the foreshock edge toward the central foreshock, in other words toward regions connected to more quasi-parallel shock con gurations, the suprathermal ion density increases progressively in both runs (marked by the hatched black and purple bars), consistent with previous studies [see Burgess et al. 2012, and references therein]. The larger breadth of the foreshock in Run 2, as well as the slightly higher suprathermal ion density in the outermost regions, can most likely be ascribed to the atter bow shock shape, which results in the associated B_n being lower in Run 2 than in Run 1 at a given position in the foreshock. In Run 1 (black curve), the central foreshock is bounded by two ridges of higher suprathermal ion density, forming a peak and a plateau in the dawnward and duskward edges of the foreshock, respectively (indicated by the black bars in Fig. 3a). These features correspond to the bands of enhanced n_{beam} identi ed in Fig. 2c. Inward of these ridges, the suprathermal ion density decreases toward the central foreshock. In Run 2, on the other hand, the smooth increase of n_{beam} from the edge of the foreshock inward ends at a value comparable to that found in the central foreshock (purple curve). Panels b, c and d of Fig. 3 display the total ion density, the magnetic eld strength normalized to the IMF strength B/B_{IMF}, and the amplitude of the uctuations dB, $dB = |B - \langle B \rangle| = B_{IMF}$. These parameters all indicate that the suprathermal ion ridges are located just outside of the region of the foreshock populated by highly compressive waves. This is particularly well illustrated by dB which increases signi cantly in the inner part of both ridges. We also note that when entering the foreshock from the duskward edge, we observe correlated enhancements in the magnetic eld magnitude and plasma density, which then decrease below their initial values. This is consistent with the crossing of the foreshock compressional boundary, which marks the entry into the region of the ULF foreshock where compressive waves develop [e.g. Omidi et al, 2009; Rojas-Castillo et al. 2013; Kajdi£ et al, 2017]. We propose the following scenario for the

formation of the ridges. As mentioned above, the density of eld-aligned beams increases when moving toward smaller $_{Bn}$ values. At some point, ULF waves start to develop from the ion-ion beam instability and alter in return the suprathermal ion population. Small amplitude waves only weakly modify the ion distribution functions, thus creating the plateau-like structure in the duskward foreshock. However, as the waves become more compressive, they scatter much more e ciently the ions and result in a decrease of the suprathermal ion density toward the central foreshock. Because the amplitude of the waves is larger closer to the edge of the dawnward foreshock, only a peak and not a plateau is observed there.

Clearly, the variation of the IMF strength a ects the development of this ridge of suprathermal ions at the edge of the ULF foreshock. The di erent Mach numbers and plasma simply that the shock structure di ers between the two runs. This is also expected to a ect the fraction of shock-re ected ions, resulting in a higher suprathermal ion density in Run 1 than in Run 2 for a given $_{Bn}$. This explains the much larger n_{beam} at the edge of the ULF foreshock in Run 1. Furthermore, Figure 3d shows that the amplitude of the ULF waves is signi cantly lower in Run 2, and is roughly the same across the ULF foreshock. We do not observe clear signatures of the foreshock compressional boundary, in agreement with the work by Omidi et al. [2009] which showed that it becomes weaker when the Mach number decreases, and thus implies that the foreshock waves become less compressive. Therefore, with only small amplitude waves throughout the ULF foreshock, the suprathermal ions would not experience increased scattering in the central foreshock, which could explain the relatively constant n_{beam} along the cut through the foreshock in Run 2 (see the purple line in Fig. 3a).

3.3 Foreshock wave properties

To investigate the foreshock ULF wave properties, we extract time series of data at 30 locations in the foreshock indicated by the plus signs in Fig. 1a and 1b. We apply a wavelet transform [Torrence and Compo, 1998] using a Morlet mother waveform to each magnetic eld component of each time series. The wavelet transform was chosen because it allows to investigate the temporal variation of the wave activity. We then compute the total power spectrum density (PSD) of the uctuations, as de ned for example in Pitna et al. [2016]. The peaks of the PSD yield the period of the dominant wave modes, while the wavelet power spectra show how these evolve over time. As an example, Fig. 4a-c show case B_z component of the magnetic eld at the virtual spacecraft A located at (x = 35 R_E, y = 10 R_E) in Run 1, its color-coded wavelet power spectrum as a function of time and period, and the total PSD over the entire considered interval. The hatched part of the wavelet power spectrum corresponds to the region below the cone of in uence, where edge e ects become important, and is thus not taken into account when computing the PSD. Black contours indicate the 95% con dence level. The wavelet power spectrum in Fig. 4b shows that there is essentially one predominant wave mode, with a period of about 34 s according to the PSD, corresponding to the 30 s foreshock wave [Eastwood et al., 2005a], as was already shown in Palmroth et al. [2015].

3.3.1 Wave modes

The distribution of the number of wave modes in the foreshock is illustrated in Fig. 1a and b, where the white and pink plus signs indicate single-peaked and double-peaked B_z PSD, respectively. Secondary peaks are considered signi cant when they reach at least 40% of the maximum PSD, as was done in Palmroth et al. [2015]. In Run 1, the wavelet spectrograms and associated PSD obtained for each of the virtual spacecraft indicated in Fig. 1a reveal that the foreshock is mostly permeated by quasi-monochromatic waves (white plus signs in Fig. 1a). When moving closer to the bow shock, the magnetic eld uctuations become more irregular, especially on the B_x component (not shown), resulting in more complex wavelet spectra indicating the coexistence of several wave modes (pink plus signs in Fig. 1a). This is consistent with spacecraft observations which show that complicated wave patterns due to intricate wave-particle interactions are found in the innermost part of the fore-

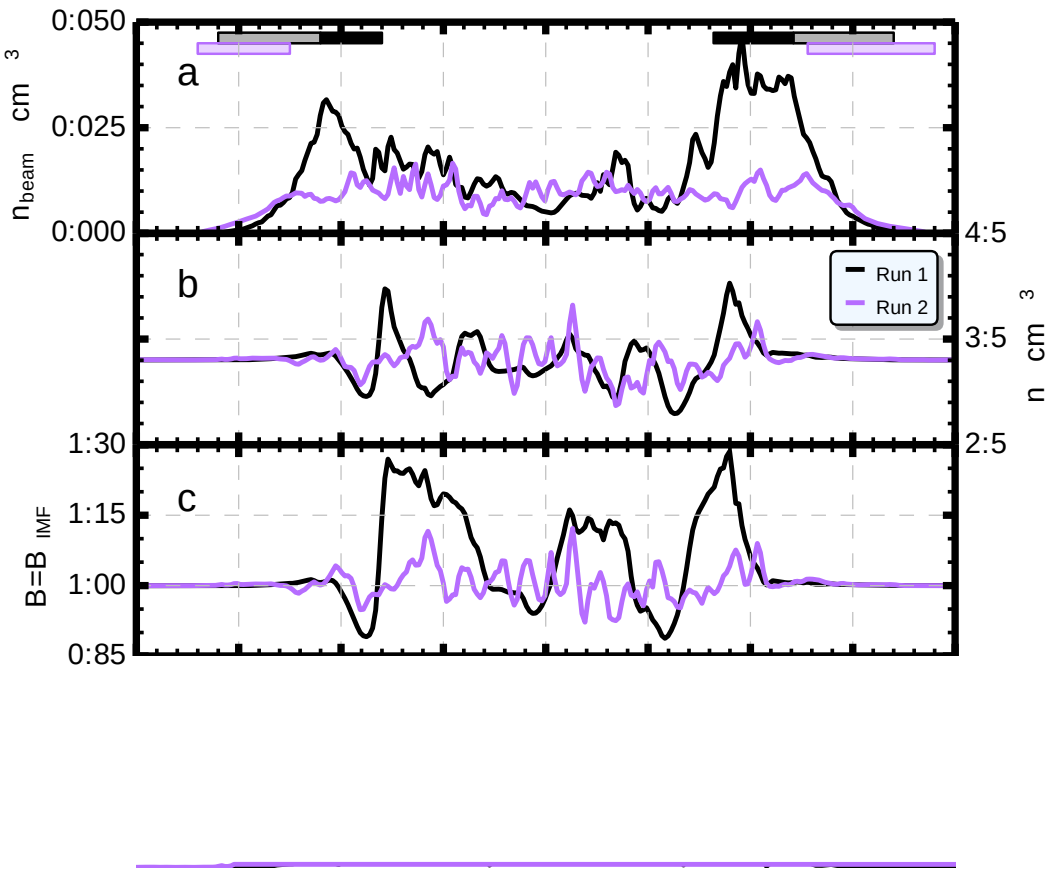

Figure 3. From top to bottom: (a) suprathermal ion density, (b) total ion density, (c) magnetic field strength normalized to the IMF strength and (d) $\delta B/B = j(B - B_{IMF})j/B_{IMF}$ in Run 1 (black) and Run 2 (purple) along a cut line through the foreshock at $x = 30\ R_E$. The black bars in panel (a) indicate the suprathermal ion ridges in Run 1, and the hatched bars show the regions where the suprathermal ion density increases progressively in Run 1 (black) and Run 2 (purple).

Figure 4. Wave activity at ($x = 35\,R_E$, $y = -10\,R_E$) in Run 1. From top to bottom: (a) time series of the magnetic eld B_z component, (b) its associated wavelet power spectrum and (c) total power spectrum density over the whole interval. The black contours in panel (c) outline the 95% con dence level, while the hatched area is below the cone of in uence.

shock, populated by di use ions, while quasi-monochromatic ULF waves are observed in the outer foreshock [see, e.g., Hoppe and Russell, 1983; Eastwood et al., 2005; Hobara et al., 2007]. Similarly, the wave activity grows in complexity toward the shock in Run 2. The two runs di er however in that some PSDs display two predominant peaks also farther out in the foreshock in Run 2 (pink plus signs in Fig. 1b), one at a period around 17 s and the other around 10 s. Similar results are obtained with the other magnetic eld components. Clearly, there is an additional wave mode growing in a large fraction of the foreshock in Run 2, which does not develop in Run 1.

Both wave modes are for example observed in Run 2 by virtual spacecraft B positioned at ($x = 25\,R_E$, $y = 10\,R_E$), as shown by the time series of B_z displayed in Fig. 5a and its associated wavelet spectrogram and PSD (Fig. 5b and c). Initially, only waves with a period around 17 s are present, but progressively the 10 s waves grow and both modes coexist during most of the displayed interval. The 10 s waves become predominant between $t = 480$ s and $t = 510$ s. The fact that the wave activity changes with time at a given location in the foreshock is probably related to the outward motion of the bow shock in our 2D setup. Here we concentrate on identifying the wave modes and what changes in the local foreshock parameters result in the appearance of the second type of waves. Using minimum variance analysis [see, for example, Sonnerup and Scheible, 1998], which allows to identify the direction in which the uctuations of one parameter minimize, we determine the direction of the wave vector on two sub-intervals, depicted by the black rectangles in Fig. 5a, each corresponding to one of the wave modes being dominant. For both intervals, the ratio of intermediate to minimum eigenvalues is above 10, meaning that the minimum variance direction, which is the wave vector direction, is well-de ned [Eastwood et al., 2005]. Note however that the maximum and intermediate variance directions are degenerate. We nd that the 17 s waves propagate at about 30 from the magnetic eld direction, while the 10 s waves are more parallel-propagating, with $_{kB}$ 6 . We then project the magnetic eld into a frame de ned by the wave vector k and two perpendicular directions forming a right-handed triplet, and plot its two perpendicular components as a function of each other, in order to examine the polarisation of the waves. Figures 5d and e reveal that the waves are left-handed in the simulation frame during both intervals. This polarisation is consistent with that of magnetosonic waves generated by the ion-ion beam right-hand instability which propagate toward the upstream parallel to the beam and therefore appear as left-handed in the simulation frame [Hoppe and Russell, 1983]. This suggests that the same type of instability generates magnetosonic waves with two di erent periods. The resonance condition of this mode is given by

$$! = V_{beam}k_k \quad _{ci} \tag{1}$$

where V_{beam} is the beam velocity and $_{ci}$ is the ion gyrofrequency, showing that the period of the waves is mainly controlled by the beam speed [see, Eastwood et al., 2005].

Figure 5f and g display two ion velocity distribution functions (VDF) taken at ($x = 24.3\,R_E$, $y = 9.8\,R_E$), which is the nearest cell to virtual spacecraft B where VDFs were recorded, at two di erent times in the run. Color-coded is the phase space density in the (V_k,$V_?$) plane (relative to the magnetic eld), computed from the 3D VDF as if it was scanned by the electrostatic analyser [McFadden et al., 2008] onboard the THEMIS satellites [Angelopoulos, 2008], in order to facilitate comparison with typical VDFs in spacecraft measurements. To do so, we consider that the spin axis of the spacecraft is normal to the (V_k,$V_?$) plane, and we integrate the phase space density within 6 the opening angle of the instrument. Panel 5f, at $t = 350$ s, showcases a typical eld-aligned beam, with the solar wind core on the left side of the plot. This distribution coincides with the time when a single wave mode starts to develop at virtual spacecraft B. As time proceeds, the beam parallel velocity decreases, likely because of energy loss through the production of ULF waves, while a second beam, with a higher parallel speed, appears and grows. At $t = 480$ s, when the wave activity is stronger and covers a broad range of periods, with two peaks around 11 s and 17 s (see Fig. 5b), the VDF comprises two populations of backstreaming suprathermal ions. Because of their di erent parallel velocities, each of these beams may excite magnetosonic

Figure 5. Wave activity at ($x = 25\,R_E$, $y = -10\,R_E$) in Run 2. (a) time series of the magnetic eld B_z component, (b) its associated wavelet power spectrum and (c) total power spectrum density over the whole interval. Hodograms of the waves in the plane perpendicular to the wave vector between $t = 350$ s and $t = 400$ s (d) and $t = 480$ s and $t = 510$ s (e) and ion VDFs at times $t = 350$ s (f) and $t = 480$ s (g). In panels d and e, the average magnetic eld is pointing toward the reader. The black bars in panel (a) indicate the intervals on which minimum variance analysis is applied and from which panels (d) and (e) are constructed.

waves at di erent frequencies through the right-hand resonant ion-ion beam instability (see Eq. 1). Closer to the bow shock ($x \sim -20\,R_E$), the VDFs display the characteristics of intermediate or di use distributions, covering a much broader range of pitch angles (not shown). Therefore, some of the waves observed there might be caused by other instabilities. In particular, spacecraft observations have shown that other types of waves, such as Alfvén modes, can develop in conjunction with di use ions [Eastwood et al., 2003]. In Run 1, the only location at which two modes are present is also associated with intermediate ion distributions. Farther out in the foreshock, we mostly encounter eld-aligned beams, with only one suprathermal ion population. This may explain why only quasi-monochromatic waves permeate the foreshock in Run 1, while they develop at multiple frequencies in Run 2.

In order to check whether two beams at di erent parallel velocities can excite magnetosonic waves with distinct frequencies, we use the Waves in Homogeneous Anisotropic Magnetized Plasmas code [WHAMP, https://github.com/irfu/whamp, Rönnmark, 1982; Kempf et al., 2013] to characterize the fastest growing wave modes. We use as inputs to the code three ion populations: one with parameters representative of the in owing solar wind and two corresponding to the two beams in Fig. 5g, with velocities $V_{beam1} = 400\,\mathrm{km\,s^{-1}}$ and $V_{beam2} = 1200\,\mathrm{km\,s^{-1}}$ and densities $n_{beam1} = 7 \cdot 10^{3}\,\mathrm{m^{-3}}$ and $n_{beam2} = 3 \cdot 10^{3}\,\mathrm{m^{-3}}$. We nd that the maximum growth rate of the waves is in the k_x direction. Figure 6 shows the dispersion relation obtained from WHAMP in the $\omega(k_x)$ plane. The color scheme indicates the growth rate and shows that it maximizes in two parts of the dispersion relation, around $\omega = \omega_{ci} = 0.3$ and $\omega = \omega_{ci} = 0.55$. This corresponds to periods of 21 s and 12 s, respectively. This is comparable to the periods of the waves found in the simulation, which supports our interpretation that the multiple ion beams are the source of the magnetosonic waves at di erent frequencies.

3.3.2 Wave periods

In order to compare our simulation results with observations, we calculate the average period of the dominant wave mode in the foreshock. To do so, we extract the period associated with each signi cant peak of the PSD for all 30 virtual spacecraft and all three magnetic eld components. This allows us to build histograms of the wave periods for both runs, which are shown in Fig. 7. The variation of the wave period within the foreshock, despite the steady upstream conditions, is due to the variability of the beam velocity [Palmroth et al., 2015]. The median periods are very similar for all three components in a given run, about 36 s in Run 1 and 16 s in Run 2. The period of the waves is thus roughly divided by two when doubling the IMF strength, consistent with early spacecraft observations [Hoppe and Russell, 1982]. Note that we included here all signi cant peaks of the PSD. Retaining only the dominant period at each virtual spacecraft led to changes of less than 1 s in the median periods. The empirical formula derived by Le and Russell [1996], $f\,(\mathrm{mHz}) = (0.72 + 4.67 \cos\theta_{Bx})\,B\,(\mathrm{nT})$, yields the following predicted periods: $T\,(\mathrm{Run\ 1}) = 37\,\mathrm{s}$ and $T\,(\mathrm{Run\ 2}) = 19\,\mathrm{s}$, which are very close to our results. The wave periods estimated using the Takahashi et al. [1984] model, $\omega = \omega_{ci}(1 - M_A \cos\theta_{Bx})/(1 - 2M_A/\theta_{Bx})$ are $T\,(\mathrm{Run\ 1}) = 28\,\mathrm{s}$ and $T\,(\mathrm{Run\ 2}) = 15\,\mathrm{s}$. These are slightly lower than in our simulation for Run 1, but still in reasonable agreement. This slight discrepancy might be due to the fact that the foreshock waves are assumed to be generated by protons re ected at the bow shock nose in the Takahashi et al. [1984] model, whereas particle re ection occurs over a large fraction of the bow shock in our simulations. Overall, the evolution of the periods of the foreshock waves as a function of the IMF strength is well reproduced by our model.

3.3.3 Growth rate

As mentioned in Section 3.1, the foreshock appears to be broader in Run 2 than in Run 1. This might be due to a larger growth rate of the foreshock waves in Run 2, since the growth rate of the waves a ects the location of the foreshock ULF boundary [Eastwood et al., 2005a]. The eld-aligned beams would then need to travel a shorter distance before the

Figure 6. Dispersion relation of the parallel-propagating waves as determined from WHAMP. The color code indicates the growth rate. r_L is the Larmor radius of the solar wind ions.

Figure 7. Histograms of the wave periods in Run 1 (green) and Run 2 (purple), as obtained from a wavelet transform applied to the magnetic eld B_x (a), B_y (b) and B_z (c) components. The median period and its associated standard deviation in each run are indicated on the panels.

Figure 8. Growth rate of the foreshock waves. (a) Time series of the magnetic eld component, as determined from MVA, at ($x = 35\ R_E$, $y = 5\ R_E$). The red plus signs indicate the extrema of the uctuations with increasing amplitude. (b) Fit of the extrema of as a function of the growth rate $\exp(\ t)$. (c) Histograms of the growth rates in Run 1 (green) and Run 2 (purple). The median growth rate and its associated standard deviation in each run are indicated.

waves grow signi cantly. The earlier development of the waves would result in the ULF foreshock extending farther out. In order to test this hypothesis, we evaluate the growth rate of the magnetosonic waves as they are the predominant wave mode across the foreshock. This parameter can be estimated in the simulation at the time when the waves start to appear at a given location in the foreshock. As was done for the wave period, we extract time series of the magnetic eld uctuations at di erent locations in the foreshock. Since we focus here on the 30 s waves, we exclude the region close to the bow shock where other wave modes can also develop ($x < 30\ R_E$). Furthermore, we require that the waves are nearly sinusoidal when they start to grow and that they display at least ve consecutive extrema with increasing amplitude (in absolute value), in order to obtain a reasonable t quality when estimating the growth rate. We then perform a minimum variance analysis on the magnetic eld time series of each virtual spacecraft and retain those for which the determination of the minimum variance direction was reliable, i.e. when the ratio of intermediate to minimum eigenvalues was larger than 10 [Eastwood et al., 2005b]. The magnetic eld components are calculated in the minimum variance frame, where B_n is parallel to the wave vector (minimum variance direction), and B_l and B_m along the maximum and intermediate variance directions, respectively. The sinusoidal waves being essentially transverse [see, e.g., Le et al, 1992; Blanco-Cano et al., 2006], we use the B_l and B_m components to determine the growth rate, as exempli ed in Fig. 8 with the B_l component at position x (= 35 R_E, y = 5 R_E) in Run 1. We identify the extrema of the magnetic eld component time series (red plus signs) until the amplitude of the wave stops increasing and t their absolute values with an exponential function $\exp(\ t)$, where t is the time and the growth rate (blue curve in Fig. 8b). The quality of the growth rate estimate is evaluated using the 95% con dence interval. If the length of the 95% con dence interval is greater than 50% of the value of the growth rate, we consider that the growth rate is not reliable and discard it.

Histograms of the growth rates thus obtained in the foreshock of Run 1 (in green) and Run 2 (in purple) are displayed in Fig. 8c. The median growth rate in Run 1 is $0.019\ s^{-1}$ and $0.037\ s^{-1}$ in Run 2, that is about 1.9 times higher. This could then explain the broader ULF foreshock in Run 2. Gary [1993] has shown that the maximum growth rate $_{max}$ of the ion-ion right-hand resonant instability, in the direction parallel to the magnetic eld, is:

$$\frac{_{max}}{_{ci}} \ , \quad \frac{n_b}{2n_e}^{1=3} \tag{2}$$

where $_{ci}$ is the plasma gyrofrequency, n_b the beam density and n_e the electron density. $_{ci}$ is twice as large in Run 2 than in Run 1 because the IMF strength is doubled, while the beam density is about 2 to 3 times lower in the region where the waves start to develop (see Fig. 2b), which corresponds to the outer parts of the ridges we investigated in Section 3.2. According to Eq. 2, the growth rate should therefore be 1.4 to 1.6 larger in Run 2 than in Run 1. Our estimate of the variation of the growth rate from one run to the other is therefore in reasonable agreement with theoretical expectations. The discrepancy might be due to the fact that the formula established by Gary [1993] is valid for beam densities ranging between 1 and 10% of the total ion density, whereas they are below 1% at the locations where the growth rate was determined. Also, the growth rate varies signi cantly across the foreshock, in particular in Run 2 (see Fig. 8c), due to larger variations in the suprathermal ion density. This can also introduce errors in the estimate of the growth rate variation from Run 1 to Run 2.

A recent study by Dorfman et al. [2017] provides an observational estimate of the growth rate of the ULF waves in the terrestrial foreshock, using data from the ARTEMIS mission around the Moon [Angelopoulos, 2011]. The spacecraft, initially located outside of the foreshock, moved inside the ULF foreshock after a change in the IMF direction. From the variation of the amplitude of the waves from one satellite to the other, Dorfman et al. [2017] estimated the growth rate to be $= _{ci} = 0.035$. The median normalized growth rates in our simulations, $= _{ci} = 0.042$ for Run 1 and $= _{ci} = 0.041$ for Run 2, are very comparable

to the observational estimate, despite the very di erent solar wind conditions at the time of ARTEMIS measurements.

4 Summary and discussion

In this paper, we have presented a detailed study of the e ects of the IMF strength on the foreshock properties using global hybrid-Vlasov simulations. As expected from early spacecraft observations at di erent planetary foreshocks, the frequency of the ULF waves is roughly proportional to the IMF strength [Hoppe and Russell, 1982], resulting in wavelengths halved in Run 2 compared to Run 1. The modi cation of the wave frequency can have a direct impact on the wave activity inside the magnetosphere because foreshock ULF waves are thought to be the main source of magnetospheric Pc3 4 pulsations [Takahashi et al., 1984; Villante et al., 2011; Francia et al., 2012]. Furthermore, the transverse extent of the wave fronts is much smaller when the wavelength is shorter. The shock rippling, which is known to be modulated by the foreshock ULF waves [Greenstadt and Mellott, 1985; Burgess, 1995], may therefore occur at smaller scales in Run 2. This is probably interconnected with the structuring of the foreshock around the so-called spines, where the obliquity of the waves changes. The spines being more numerous and more closely spaced in Run 2, the wave fronts are smaller.

The change in the IMF strength also a ects the growth rate of the instability which triggers the magnetosonic waves permeating most of the foreshock. The broader foreshock in Run 2 implies that a larger fraction of the magnetosheath, and therefore of the magnetosphere, is located downstream of the ULF foreshock. Russell et al. [1983] have shown that waves reaching the subsolar magnetopause propagate to lower L-values than those reaching other parts of the magnetopause. For a quasi-radial IMF orientation as presented here, the broadening of the foreshock may not a ect signi cantly the transmission of the uctuations into the inner magnetosphere because the foreshock is upstream of the subsolar point. However, for other IMF orientations, a broader ULF foreshock may extend to magnetosheath streamlines connected with the subsolar region, thus allowing the waves to be transmitted deeper into the magnetosphere when the IMF strength is enhanced.

We found that at higher IMF strength, magnetosonic waves can develop at distinct frequencies in some parts of the foreshock. This was attributed to the presence of several backstreaming populations with di erent velocities. This is further supported by the results from the WHAMP code with two backstreaming ion beams. The origin of the second population, while only one beam is seen in Run 1, is however not completely clear. They may either be generated already at the bow shock, from a second re ection at the shock surface after having been advected back to it, or result from wave-particle interactions in the foreshock. The di erent plasma in the two runs may play a role in this, as they result in di erent shock properties, which could a ect the generation of eld-aligned beams. Meziane et al. [2011] reported observations from the Cluster spacecraft of multiple eld-aligned beams resembling those in our simulation. The authors suggested that the anomalous population could be produced by local changes of the quasi-parallel shock surface due to foreshock ULF waves or plasma structures. This could be further investigated in our runs but lies beyond the scope of this paper.

Additionally, we found that the bow shock shape and position change very little from one run to the other. This is attributed to the quasi-radial IMF orientation and the relatively high Mach numbers, and is consistent with MHD predictions. This suggests that despite kinetic e ects being prominent in the quasi-parallel shock regime, they may not a ect significantly the overall shock position and shape, and an MHD description may be su cient to capture them. The similar bow shocks facilitated the comparison of the two simulation runs, but it would be interesting to investigate the response of the bow shock for di erent IMF orientations. A preliminary analysis of another set of runs with more oblique IMF compared to

that analyzed here con rmed that the quasi-perpendicular bow shock retreats farther sunward than its quasi-parallel region when decreasing the M_A (not shown).

Finally, we identi ed new large-scale foreshock structures, namely two bands of enhanced suprathermal ion density anking the central foreshock, and proposed a scenario to explain their formation. In these structures, the suprathermal ion density is maximized because of the value of the θ_{Bn} angle at the bow shock, while we attribute the decrease of suprathermal ion density in the central foreshock to enhanced scattering due to the compressional waves found in this region. They seem to be colocated with the foreshock compressional boundary [Omidi et al, 2009], and their disappearance at lower M_A further supports that they are another signature of the same phenomenon, previously undetected because the suprathermal ion density is not readily obtained from spacecraft data. Revisiting the observed crossings of the foreshock compressional boundary could test this hypothesis.

Despite being restricted to 2D in real space, our simulation results show very good agreement with previous studies, suggesting that the addition of a third dimension would not change fundamentally the main foreshock properties in the simulation. Since no comparative study of 2D and 3D simulations of the foreshock has been carried so far, estimating how the 3D would a ect them precisely can only be speculative. It is however expected that the wave activity will become even more complex in 3D.

In conclusion, a change in the IMF strength alters signi cantly the foreshock properties both at large and small scales, which can in turn a ect the regions downstream of the quasi-parallel shock. The wave properties are of particular importance because foreshock uctuations can be transmitted into the inner magnetosphere. The enhanced IMF case studied here is representative of the magnetic eld strength encountered during interplanetary coronal mass ejections or magnetic clouds. It can be regarded as a snapshot of the foreshock during one such event, since the solar wind parameters are generally quasi-steady inside these transients, even though it must be noted that not only the IMF strength changes during such events. This suggests that the foreshock can di er signi cantly from its normal state in these conditions. High IMF strengths can also be typical solar wind conditions for other planets such as Mercury or exoplanets orbiting close to their host star. The present study can therefore serve as a basis to understand other planetary foreshocks, and may for example help interpreting the data from the upcoming BepiColombo mission at Mercury.

Acknowledgments

This project has received funding from the European Union's Horizon 2020 research and innovation programme under the Marie Sklodowska-Curie grant agreement No 704681. We acknowledge the European Research Council for Starting grant 200141-QuESpace, with which Vlasiator was developed, and Consolidator grant 682068-PRESTISSIMO awarded to further develop Vlasiator and use it for scienti c investigations. The CSC - IT Center for Science in Finland is acknowledged for the Pilot run and the Grand Challenge award leading to the results shown here. We thank S. von Alfthan for his major contribution in the development of Vlasiator. Data shown in this paper can be accessed by following the data policy on our web page http://www.physics.helsinki. /vlasiator/rules.php.

References

Andrés, N., K. Meziane, C. Mazelle, C. Bertucci, and D. Gómez (2015), The ULF wave foreshock boundary: Cluster observations, Journal of Geophysical Research (Space Physics) 120, 4181 4193, doi:10.1002/2014JA020783.

Angelopoulos, V. (2008), The THEMIS Mission, Space Sci. Rev., 141, 5 34, doi: 10.1007/s11214-008-9336-1.

Angelopoulos, V. (2011), The ARTEMIS Mission, Space Science Reviews, 165, 3 25, doi: 10.1007/s11214-010-9687-2.

Archer, M., T. S. Horbury, E. A. Lucek, C. Mazelle, A. Balogh, and I. Dandouras (2005), Size and shape of ULF waves in the terrestrial foreshock, Journal of Geophysical Research (Space Physics), 110, A05208, doi:10.1029/2004JA010791.

Blanco-Cano, X., N. Omidi, and C. T. Russell (2006), Macrostructure of collisionless bow shocks: 2. ULF waves in the foreshock and magnetosheath, Journal of Geophysical Research (Space Physics), 111, A10205, doi:10.1029/2005JA011421.

Blanco-Cano, X., N. Omidi, and C. T. Russell (2009), Global hybrid simulations: Foreshock waves and cavitons under radial interplanetary magnetic eld geometry, Journal of Geophysical Research (Space Physics), 114, A01216, doi:10.1029/2008JA013406.

Burgess, D. (1995), Foreshock-shock interaction at collisionless quasi-parallel shocks, Advances in Space Research, 15, 159 169, doi:10.1016/0273-1177(94)00098-L.

Burgess, D. (1997), What do we really know about upstream waves?, Advances in Space Research, 20, 673 682, doi:10.1016/S0273-1177(97)00455-9.

Burgess, D., E. Möbius, and M. Scholer (2012), Ion Acceleration at the Earth's Bow Shock, Space Science Reviews, 173, 5 47, doi:10.1007/s11214-012-9901-5.

Cairns, I. H., and C. L. Grabbe (1994), Towards an MHD theory for the stando distance of Earth's bow shock, Geophys. Res. Lett., 21, 2781 2784, doi:10.1029/94GL02551.

Chapman, J. F., and I. H. Cairns (2004), Modeling of Earth's bow shock: Application, Geophys. Res., 109, A11202, doi:10.1029/2004JA010540.

Dorfman, S., H. Hietala, P. Astfalk, and V. Angelopoulos (2017), Growth rate measurement of ulf waves in the ion foreshock, Geophysical Research Letters, 44(5), 2120 2128, doi:10.1002/2017GL072692, 2017GL072692.

Eastwood, J. P., A. Balogh, E. A. Lucek, C. Mazelle, and I. Dandouras (2003), On the existence of Alfvén waves in the terrestrial foreshock, Annales Geophysicae, 21, 1457 1465, doi:10.5194/angeo-21-1457-2003.

Eastwood, J. P., E. A. Lucek, C. Mazelle, K. Meziane, Y. Narita, J. Pickett, and R. A. Treumann (2005a), The Foreshock, Space Science Reviews, 118, 41 94, doi:10.1007/s11214-005-3824-3.

Eastwood, J. P., A. Balogh, E. A. Lucek, C. Mazelle, and I. Dandouras (2005b), Quasi-monochromatic ULF foreshock waves as observed by the four-spacecraft Cluster mission: 2. Oblique propagation, Journal of Geophysical Research (Space Physics), 110, A11220, doi:10.1029/2004JA010618.

Eastwood, J. P., A. Balogh, E. A. Lucek, C. Mazelle, and I. Dandouras (2005), Quasi-monochromatic ulf foreshock waves as observed by the four-spacecraft cluster mission: 1. statistical properties, Journal of Geophysical Research: Space Physics, 110(A11), n/a n/a, doi:10.1029/2004JA010617, a11219.

Francia, P., M. Regi, M. De Lauretis, U. Villante, and V. A. Pilipenko (2012), A case study of upstream wave transmission to the ground at polar and low latitudes, Journal of Geophysical Research (Space Physics), 117, A01210, doi:10.1029/2011JA016751.

Fuselier, S. A. (1995), Ion distributions in the Earth's foreshock upstream from the bow shock, Advances in Space Research, 15, 43 52, doi:10.1016/0273-1177(94)00083-D.

Gary, S. P. (1991), Electromagnetic ion/ion instabilities and their consequences in space plasmas - A review, Space Science Reviews, 56, 373 415, doi:10.1007/BF00196632.

Gary, S. P. (1993), Theory of Space Plasma Microinstabilities, 193 pp.

Greenstadt, E. W., and M. M. Mellott (1985), Variable eld-to-normal angles in the shock foreshock boundary observed by ISEE 1 and 2, Geophysical Research Letters, 12, 129 132, doi:10.1029/GL012i003p00129.

Greenstadt, E. W., G. Le, and R. J. Strangeway (1995), ULF waves in the foreshock, Advances in Space Research, 15, 71 84, doi:10.1016/0273-1177(94)00087-H.

Hobara, Y., S. N. Walker, M. Balikhin, O. A. Pokhotelov, M. Dunlop, H. Nilsson, and H. RèMe (2007), Characteristics of terrestrial foreshock ULF waves: Cluster observations, Journal of Geophysical Research (Space Physics), 112, A07202, doi:10.1029/2006JA012142.

Hoilijoki, S., M. Palmroth, B. M. Walsh, Y. Pfau-Kempf, S. von Alfthan, U. Ganse, O. Hannuksela, and R. Vainio (2016), Mirror modes in the Earth's magnetosheath: Results from a global hybrid-Vlasov simulation, Journal of Geophysical Research (Space Physics), 121, 4191 4204, doi:10.1002/2015JA022026.

Hoilijoki, S., U. Ganse, Y. Pfau-Kempf, P. A. Cassak, B. M. Walsh, H. Hietala, S. von Alfthan, and M. Palmroth (2017), Reconnection rates and X line motion at the magnetopause: Global 2D-3V hybrid-Vlasov simulation results, Journal of Geophysical Research (Space Physics), 122, 2877 2888, doi:10.1002/2016JA023709.

Hoppe, M. M., and C. T. Russell (1982), Particle acceleration at planetary bow shock waves, Nature, 295, 41, doi:10.1038/295041a0.

Hoppe, M. M., and C. T. Russell (1983), Plasma rest frame frequencies and polarizations of the low-frequency upstream waves: Isee 1 and 2 observations, Journal of Geophysical Research: Space Physics, 88(A3), 2021 2027, doi:10.1029/JA088iA03p02021.

Hoppe, M. M., C. T. Russell, L. A. Frank, T. E. Eastman, and E. W. Greenstadt (1981), Upstream hydromagnetic waves and their association with backstreaming ion populations - ISEE 1 and 2 observations, J. Geophys. Res., 86, 4471 4492, doi:10.1029/JA086iA06p04471.

Hsieh, W.-C., and J.-H. Shue (2013), Dependence of the oblique propagation of ULF foreshock waves on solar wind parameters, Journal of Geophysical Research (Space Physics), 118, 4151 4160, doi:10.1002/jgra.50225.

Jarvinen, R., R. Vainio, M. Palmroth, L. Juusola, S. Hoilijoki, Y. Pfau-Kempf, U. Ganse, L. Turc, and S. von Alfthan (2018), Ion Acceleration by Flux Transfer Events in the Terrestrial Magnetosheath, Geophys. Res. Lett., 45, 1723 1731, doi:10.1002/2017GL076192.

Kajdi£, P., X. Blanco-Cano, N. Omidi, D. Rojas-Castillo, D. G. Sibeck, and L. Billingham (2017), Traveling Foreshocks and Transient Foreshock Phenomena, Journal of Geophysical Research (Space Physics), 122, 9148 9168, doi:10.1002/2017JA023901.

Karimabadi, H., V. Roytershteyn, H. X. Vu, Y. A. Omelchenko, J. Scudder, W. Daughton, A. Dimmock, K. Nykyri, M. Wan, D. Sibeck, M. Tatineni, A. Majumdar, B. Loring, and B. Geveci (2014), The link between shocks, turbulence, and magnetic reconnection in collisionless plasmas, Physics of Plasmas, 21(6), 062308, doi:10.1063/1.4882875.

Kempf, Y., D. Pokhotelov, S. von Alfthan, A. Vaivads, M. Palmroth, and H. E. J. Koskinen (2013), Wave dispersion in the hybrid-Vlasov model: Veri cation of Vlasiator, Physics of Plasmas, 20(11), 112114, doi:10.1063/1.4835315.

Kempf, Y., D. Pokhotelov, O. Gutynska, L. B. Wilson III, B. M. Walsh, S. von Alfthan, O. Hannuksela, D. G. Sibeck, and M. Palmroth (2015), Ion distributions in the Earth's foreshock: Hybrid-Vlasov simulation and THEMIS observations, Journal of Geophysical Research (Space Physics), 120, 3684 3701, doi:10.1002/2014JA020519.

Kis, A., M. Scholer, B. Klecker, E. Möbius, E. A. Lucek, H. Rème, J. M. Bosqued, L. M. Kistler, and H. Kucharek (2004), Multi-spacecraft observations of di use ions upstream of Earth's bow shock, Geophys. Res. Lett., 31, L20801, doi:10.1029/2004GL020759.

Kudela, K., V. N. Lutsenko, E. T. Sarris, D. G. Sibeck, and M. Slivka (2005), DOK-2 ion uxes upstream from the bow shock: characteristics from 4 years of Interball-1 measurements, Planetary and Space Science, 53, 59 64, doi:10.1016/j.pss.2004.09.029.

Le, G., and C. T. Russell (1996), Solar wind control of upstream wave frequency, J. Geophys. Res., 101, 2571 2576, doi:10.1029/95JA03151.

Le, G., C. T. Russell, M. F. Thomsen, and J. T. Gosling (1992), Observations of a new class of upstream waves with periods near 3 seconds, Journal of Geophysical Research: Space Physics, 97(A3), 2917 2925, doi:10.1029/91JA02707.

Le, G., P. J. Chi, W. Goedecke, C. T. Russell, A. Szabo, S. M. Petrinec, V. Angelopoulos, G. D. Reeves, and F. K. Chun (2000), Magnetosphere on May 11, 1999, the day the solar wind almost disappeared: II. Magnetic pulsations in space and on the ground, Geophys. Res. Lett., 27, 2165 2168, doi:10.1029/1999GL000012.

Lin, Y., and X. Y. Wang (2005), Three-dimensional global hybrid simulation of dayside dynamics associated with the quasi-parallel bow shock, Journal of Geophysical Research

(Space Physics), 110, A12216, doi:10.1029/2005JA011243.

McFadden, J. P., C. W. Carlson, D. Larson, M. Ludlam, R. Abiad, B. Elliott, P. Turin, M. Marckwordt, and V. Angelopoulos (2008), The themis esa plasma instrument and in- ight calibration, Space Science Reviews, 141(1), 277 302, doi:10.1007/s11214-008-9440-2.

Meziane, K., A. M. Hamza, M. Wilber, C. Mazelle, and M. A. Lee (2011), Anomalous foreshock eld-aligned beams observed by Cluster, Annales Geophysicae, 29, 1967 1975, doi:10.5194/angeo-29-1967-2011.

Omidi, N., X. Blanco-Cano, and C. T. Russell (2005), Macrostructure of collisionless bow shocks: 1. Scale lengths, Journal of Geophysical Research (Space Physics), 110, A12212, doi:10.1029/2005JA011169.

Omidi, N., D. G. Sibeck, and X. Blanco-Cano (2009), Foreshock compressional boundary, Journal of Geophysical Research (Space Physics), 114, A08205, doi:10.1029/2008JA013950.

Omidi, N., D. Sibeck, X. Blanco-Cano, D. Rojas-Castillo, D. Turner, H. Zhang, and P. Kajdi£ (2013), Dynamics of the foreshock compressional boundary and its connection to foreshock cavities, Journal of Geophysical Research (Space Physics), 118, 823 831, doi:10.1002/jgra.50146.

Omidi, N., G. Collinson, and D. Sibeck (2017), Structure and Properties of the Foreshock at Venus, Journal of Geophysical Research (Space Physics), 122, 10, doi:10.1002/2017JA024180.

Palmroth, M., M. Archer, R. Vainio, H. Hietala, Y. Pfau-Kempf, S. Hoilijoki, O. Hannuksela, U. Ganse, A. Sandroos, S. v. Alfthan, and J. P. Eastwood (2015), Ulf foreshock under radial imf: Themis observations and global kinetic simulation vlasiator results compared, Journal of Geophysical Research: Space Physics, 120(10), 8782 8798, doi:10.1002/2015JA021526, 2015JA021526.

Palmroth, M., S. Hoilijoki, L. Juusola, T. I. Pulkkinen, H. Hietala, Y. Pfau-Kempf, U. Ganse, S. von Alfthan, R. Vainio, and M. Hesse (2017), Tail reconnection in the global magnetospheric context: Vlasiator rst results, Annales Geophysicae, 35, 1269 1274, doi:10.5194/angeo-35-1269-2017.

Perrone, D., O. Alexandrova, A. Mangeney, M. Maksimovic, C. Lacombe, V. Rakoto, J. C. Kasper, and D. Jovanovic (2016), Compressive Coherent Structures at Ion Scales in the Slow Solar Wind, The Astrophysical Journal, 826, 196, doi:10.3847/0004-637X/826/2/196.

Petrukovich, A. A., T. Inamori, J. Balaz, K. Kudela, M. Slivka, I. Strharsky, V. A. Gladyshev, T. Sarris, and E. Sarris (2015), Oscillations of energetic ions ux near the Earth's bow shock, Journal of Geophysical Research (Space Physics), 120, 4700 4710, doi:10.1002/2015JA021077.

Petrukovich, A. A., O. M. Chugunova, T. Inamori, K. Kudela, and J. Stetiarova (2017), Foreshock waves as observed in energetic ion ux, Journal of Geophysical Research (Space Physics), 122, 4895 4904, doi:10.1002/2016JA023693.

Pfau-Kempf, Y. (2016), Vlasiator: from local to global magnetospheric hybrid-Vlasov simulations, Phd thesis, Finnish Meteorological Institute Contributions.

Pfau-Kempf, Y., H. Hietala, S. E. Milan, L. Juusola, S. Hoilijoki, U. Ganse, S. von Alfthan, and M. Palmroth (2016), Evidence for transient, local ion foreshocks caused by dayside magnetopause reconnection, Annales Geophysicae, 34, 943 959, doi:10.5194/angeo-34-943-2016.

Pfau-Kempf, Y., M. Battarbee, U. Ganse, S. Hoilijoki, L. Turc, S. von Alfthan, R. Vainio, and M. Palmroth (2018), On the importance of spatial and velocity resolution in the hybrid-Vlasov modeling of collisionless shocks, Frontiers in Physics - Plasma Physics, 6(44), doi:10.3389/fphy.2018.00044.

Regi, M., M. De Lauretis, and P. Francia (2014), The occurrence of upstream waves in relation with the solar wind parameters: A statistical approach to estimate the size of the foreshock region, Planetary and Space Science, 96, 100 105, doi:10.1016/j.pss.2013.10.012.

Rojas-Castillo, D., X. Blanco-Cano, P. Kajdi£, and N. Omidi (2013), Foreshock compressional boundaries observed by Cluster, Journal of Geophysical Research (Space Physics), 118, 698 715, doi:10.1029/2011JA017385.

Rönnmark, K. (1982), WHAMP Waves in Homogeneous, Anisotropic Multicomponent Plasmas, Kiruna Geophysical Institute Reports No. 179

Russell, C. T., J. G. Luhmann, T. J. Odera, and W. F. Stuart (1983), The rate of occurrence of dayside Pc 3,4 pulsations - The L-value dependence of the IMF cone angle effect, Geophys. Res. Lett., 10, 663 666, doi:10.1029/GL010i008p00663.

Schwartz, S. J., M. F. Thomsen, and J. T. Gosling (1983), Ions upstream of the earth's bow shock - A theoretical comparison of alternative source populations, J. Geophys. Res., 88, 2039 2047, doi:10.1029/JA088iA03p02039.

Sonnerup, B. U. O., and M. Scheible (1998), Analysis Methods for Multi-spacecraft Data. ISSI Scienti c Report, chap. Minimum and maximum variance analysis.

Takahashi, K., R. L. McPherron, and T. Terasawa (1984), Dependence of the spectrum of Pc 3-4 pulsations on the interplanetary magnetic eld, J. Geophys. Res., 89, 2770 2780, doi:10.1029/JA089iA05p02770.

Torrence, C., and G. P. Compo (1998), A Practical Guide to Wavelet Analysis., Bulletin of the American Meteorological Society, 79, 61 78, doi:10.1175/1520-0477(1998)079<0061:APGTWA>2.0.CO;2.

Trattner, K. J., E. Mobius, M. Scholer, B. Klecker, M. Hilchenbach, and H. Luehr (1994), Statistical analysis of di use ion events upstream of the Earth's bow shock, J. Geophys. Res., 99, 13, doi:10.1029/94JA00576.

Turc, L., D. Fontaine, P. Savoini, and R. Modolo (2015), 3D hybrid simulations of the interaction of a magnetic cloud with a bow shock, Journal of Geophysical Research (Space Physics), 120, 6133 6151, doi:10.1002/2015JA021318.

Villante, U., C. De Paulis, and P. Francia (2011), The transmission of upstream waves to the magnetosphere: An analysis at widely separated ground stations, Journal of Geophysical Research (Space Physics), 116, A06219, doi:10.1029/2010JA016263.

von Alfthan, S., D. Pokhotelov, Y. Kempf, S. Hoilijoki, I. Honkonen, A. Sandroos, and M. Palmroth (2014), Vlasiator: First global hybrid-Vlasov simulations of Earth's foreshock and magnetosheath, Journal of Atmospheric and Solar-Terrestrial Physics, 120, 24 35, doi:10.1016/j.jastp.2014.08.012.

Wilson III, L. B. (2016), Low Frequency Waves at and Upstream of Collisionless Shocks, Washington DC American Geophysical Union Geophysical Monograph Series, 216, 269 291, doi:10.1002/9781119055006.ch16.